UCLA
UCLA Electronic Theses and Dissertations

Title

Study of Four-Wave Mixing in Bulk Semiconductors Excited by GW/cm� 10 μm Laser Fields

Permalink

https://escholarship.org/uc/item/1mn445fx

Author

Matteo, Daniel Alexander

Publication Date

2019

Peer reviewed|Thesis/dissertation

UNIVERSITY OF CALIFORNIA

Los Angeles

Study of Four-Wave Mixing in Bulk Semiconductors

Excited by GW/cm^2 10 μm Laser Fields

A thesis submitted in partial satisfaction

of the requirements for the degree Master of Science

in Electrical & Computer Engineering

by

Daniel Matteo

2019

ABSTRACT OF THE THESIS

Study of Four-Wave Mixing in Bulk Semiconductors

Excited by GW/cm^2 10 μm Laser Fields

by

Daniel Matteo

Master of Science in Electrical & Computer Engineering

University of California, Los Angeles, 2019

Professor Chandra J. Joshi, Chair

Semiconductors such as GaAs, Ge, and ZnSe have long been important materials for optics and photonics applications in the middle infrared range (2-20 μm), finding use as windows or in optoelectronic devices. The nonlinear refractive index (n_2) of these three semiconductors is well documented near resonance in the near infrared, but as technology progresses to longer wavelengths and higher intensities, characterization of these materials in the long-wavelength infrared (LWIR, 8-14 μm) at GW/cm^2 intensities becomes necessary. In this thesis, we report on measurements of the effective nonlinear refractive index in GaAs, Ge, and ZnSe using four-wave mixing of a 10 μm CO_2 laser beat-wave at both high 1-10 GW/cm^2 and low 1-10 MW/cm^2 intensities, with 200 ps and 300 ns long pulses respectively. Intensity dependent nonlinear absorption is also observed. In addition, by decreasing the beat-frequency of the CO_2 laser beat-wave, the nonlinear optical response is found to increase by a factor of 10 in GaAs. Simulations attribute this beat-wave enhancement to nonlinear currents of photoexcited free carriers and predict that by further decreasing the beat frequency to a few GHz, the nonlinear optical response can be increased by a factor of almost 100. Optical control of the nonlinearity in GaAs could lead to the production of high power broadband frequency combs with narrow frequency separations ideal for high resolution spectroscopy in the LWIR.

The thesis of Daniel Matteo is approved.

Chee Wei Wong

Warren B. Mori

Chandra J. Joshi, Committee Chair

University of California, Los Angeles

2019

Dedication

To my Mom, Dad and Sister, and all the family and friends who have supported me and let me talk to them about physics. To the world around us, thank you for being so fascinating.

Contents

List of Figures

List of Tables

Acknowledgments

I would like to thank Dr. Sergei Tochitsky, whose great ideas, continuous guidance, and constant encouragement in the lab has made this work possible, as well as Professor Chan Joshi, who gave me the chance to pursue research and has guided and supported me the whole way. I would also like to thank Dr. Jeremy Pigeon for major assistance in running the experiments, and both Dr. Pigeon and Eric Welch for invaluable advice and many great discussions about physics. Finally, I would like to acknowledge Dr. Ulrich Huttner and Professor Stephan W. Koch from Philipps-Universität Marburg for their assistance in running simulations.

1 Introduction

Semiconductors have been inseparable from the fields of optics and photonics since the invention of the laser. Many of these materials are transparent throughout the middle infrared range (MIR) from 2-20 μm and are used to make various optical elements, but also give the robust ability to manipulate and detect light in the form of lasers, switches, or photodetectors. Semiconductor materials generally have high nonlinearities compared to other bulk solids, and have found broad use in nonlinear optics to generate efficient second harmonic light, supercontinuum, and for frequency conversion to downconvert ultrafast near-infrared (NIR) pulses (e.g. from Ti:Sapphire lasers) in optical parametric amplifiers. Parallel development of the semiconductor fabrication industry (motivated primarily by the desire for high speed nanoscale electronics) has allowed for the optimization of electrical and linear optical properties of semiconductors as well as the creation of structured semiconductors, which may provide very high nonlinearities originating from the spatial confinement of electrons (see e.g. Ref. [1]).

A few MIR materials stand out above the rest for many of the applications listed, including GaAs, CdTe, n-Ge, and ZnSe. These materials are rather well characterized in the near infrared, where linear and two-photon absorption dominate their linear and nonlinear optical properties [2], as well as in the MIR at low intensities ($\sim$1 MW/cm^2) [3, 4]. However, as MIR technology is being driven to longer wavelengths and higher intensities, knowledge of the nonlinear optical response of these materials to nonresonant MIR pulses with intensities >1 GW/cm^2 becomes more and more important. Although structured semiconductors provide a unique opportunity to study controllable quantum states of solids, their dielectric breakdown threshold is far lower than bulk solids, making bulk materials more viable for high intensity studies.

Recent experimental results suggest that low and high fields results in the bulk nonresonant regime may be drastically different. Whereas low intensity nonlinear optics can be described well by a perturbative expansion of the material polarization, many high field

1

interactions fundamentally break this assumption. In particular, high fields may dramatically alter the band structure of solids via the dynamical Franz-Keldysh effect [5] which can be used to induce transparency/absorption above/below the band edge in semiconductors [6, 7]. Strong nonresonant fields can also modify the wavefunctions of free electrons such that they are spatially localized and simultaneously accelerated to the outer reaches of the Brillouin zone (BZ) [8, 9]. Many inter- and intraband microscopic effects may play a role in high harmonic generation (HHG), where nonresonant radiation with intensities on the order of 1 TW/cm^2 drives an extremely nonperturbative response and emits odd (and sometimes even) harmonics up to the 19th harmonic [9–12]. Ultrabroadband HHG spectra may open the path to the study of attosecond dynamics in solids. Coherent processes such as Rabi flopping have also been observed in bulk semiconductors far away from resonance [13, 14].

As is clear, high field interactions between light and semiconductors include many diverse effects which fundamentally (and transiently) change the structure and nonlinear optical response of the solids and can be used to study the quantum structure of matter and many-body interactions. However these high field experiments all take advantage of extremely high intensities on the order of 100 GW/cm^2 or higher, very close to or above the threshold for dielectric breakdown, making them less useful for technological applications. The question then remains — to what degree do strong-field effects play a role in nonresonant interactions around 1 GW/cm^2, and can they be used to control the nonlinear optical response of semiconductors in a nondestructive way with low optical loss?

In this thesis we study the third order nonlinear optical response of the semiconductors GaAs, n-Ge, and ZnSe with 10 μm CO$_2$ laser beat-waves at high (1 GW/cm^2) intensities using four-wave mixing. We also performed similar measurements at low (1 MW/cm^2) intensities in the same materials. The structure of the thesis is as follows. Chapter 2 will introduce relevant theoretical background on both bound and free carrier nonresonant nonlinear optical responses in semiconductors, and Chapter 3 will describe the experimental setup and measurement techniques used. Chapter 4 will present the results of four-wave mixing experiments in these samples and discuss measurement of the effective nonlinear

refractive index. Chapter 5 will investigate GaAs in more depth and demonstrate a beat-wave controllable nonlinear response. Finally, Chapter 6 will give conclusions and look forward to possible further studies or applications of the results presented.

2 Theory

The macroscopic response of matter to light with an electric field $\vec{\mathscr{E}}(\vec{r}, t)$ is described by the material polarization $\vec{P}(\vec{r}, t) = \epsilon_0 \chi^{(1)} \vec{\mathscr{E}}(\vec{r}, t)$ in the low field (linear) limit. Linear optical properties of matter such as refraction and absorption are related to $\chi^{(1)}$, the magnitude of which is determined by the electromagnetic (EM) wave frequency's proximity to natural resonant frequencies of the material. These natural resonances represent a variety of different transitions between quantum states including electronic levels of an atom or rovibrational levels of a molecule. Dominant resonances in solids include absorption above the fundamental band gap ($\hbar\omega \geq E_g$) or phonon absorption. Away from a fundamental resonance, the propagation of light is still affected depending on the resonance's strength and proximity, bringing about material dispersion.

Nonlinear responses of constituent particles to the electric field begin to manifest when strong light fields are applied to a material. The basic mathematics describing nonlinear optical properties of matter are the nonlinear susceptibility tensors $\chi^{(n)}$, which can be used to expand the material polarization in orders of the electric field:

$$\vec{P} = \epsilon_0 \left[\chi^{(1)} \vec{\mathscr{E}} + \chi^{(2)} \vec{\mathscr{E}}^2 + \chi^{(3)} \vec{\mathscr{E}}^3 + \cdots \right]. \tag{1}$$

If the electric fields are harmonic optical fields

$$\vec{\mathscr{E}} = \frac{1}{2} \left[\vec{E}_0 e^{-i(\omega t - \vec{k}\cdot\vec{r})} + c.c. \right] \tag{2}$$

where $\vec{E}_0$ is the envelope of the field, it is clear to see that if a material possesses either $\chi^{(2)}$ or $\chi^{(3)}$, the polarization can oscillate with harmonic frequencies of ω (e.g. 2ω, 3ω). This polarization acts as a source term in the driven wave equation

$$\nabla^2 \vec{\mathscr{E}} - \frac{n^2}{c^2} \frac{\partial^2 \vec{\mathscr{E}}}{\partial t^2} = \frac{1}{\epsilon_0 c^2} \frac{\partial^2 \vec{P}}{\partial t^2} \tag{3}$$

3

thereby generating light at these frequencies.

Due to the polar nature of both $\vec{P}$ and $\vec{\mathcal{E}}$ and the dependence of even orders of $\vec{P}^{(n)}$ on even powers of $\vec{\mathcal{E}}$, $\chi^{(2)}$ can only be nonzero when spatial inversion symmetry is broken in a noncentrosymmetric crystal. Many common semiconductors, including III-V and II-VI binary semiconductors, are noncentrosymmetric and have strong $\chi^{(2)}$ which allows for nonlinear processes such as second harmonic generation (SHG) or difference frequency generation (DFG). In centrosymmetric crystals $\chi^{(3)}$ is the lowest order nonzero nonlinear susceptibility.

When a monochromatic EM wave with frequency ω is incident on a $\chi^{(3)}$ material, a nonlinear polarization oscillating with ω can be driven with magnitude proportional to $\chi^{(3)}|\vec{\mathcal{E}}|^2\vec{\mathcal{E}}$, which is of the same form as the linear material polarization. For a nonmagnetic material ($\mu = \mu_0$) away from resonance ($\mathrm{Im}(\epsilon) = 0$), the refractive index of a dielectric is $n = \sqrt{1 + \chi}$; in this sense, the third order polarization can be viewed as an intensity dependant correction to the linear index. A nonlinear refractive index n_2 can be defined using $n = n_0 + n_2 I$ and is related to $\chi^{(3)}$ by

$$n_2 = \frac{3}{4n_0^2\epsilon_0 c}\chi^{(3)}. \tag{4}$$

The nonlinear refractive index is a quantity of both fundamental and practical interest. It is used to characterize a variety of material responses and third-order nonlinear optical processes such as self-phase modulation (SPM) and third-harmonic generation, and also mediates self focusing (SF), all of which are fundamental drivers behind supercontinuum generation. An effective nonlinear refractive index, $n_{2,\mathrm{eff}}$, is a sum of n_2 resulting from different physical mechanisms and will be used in this thesis to compare nonlinear optical responses of semiconductors. In semiconductors, effects causing $n_{2,\mathrm{eff}}$ (or $\chi^{(3)}$) can often be generalized into two separate categories: bound electron nonlinearities and free carrier nonlinearities.

2.1   Bound Electron Nonlinearities

A Newtonian picture of the optical susceptibilities originating from bound electrons in a solid (although this model may work well for a variety of systems) can be described by a classical

electron oscillator model. In this model an electron sits at the bottom of an attractive potential around a crystal ion and is driven by a sinusoidal EM wave. The electron is found to move as a damped driven oscillator in the field with a material polarization $\vec{P} = -Ne\vec{r}$, where N is the electron density. The linearity of this system is apparent - any attractive potential may be modeled as parabolic near local minima, corresponding to a linear restoring force and purely sinusoidal response to an external sinusoidal perturbation.

Though oftentimes useful, the parabolic potential well is an approximation and real systems will have nonparabolic potentials leading to nonlinear restoring forces. The classical model can be solved with perturbation theory and has been described by many authors, including Refs. [15, 16]. Solutions give nth order polarizations oscillating at frequencies which are combinations of n incident frequencies - e.g. if EM waves at frequencies ω_1 and ω_2 are incident, $\vec{P}^{(2)}$ will oscillate at $\pm 2\omega_1$, $\pm 2\omega_2$, $\pm(\omega_1 + \omega_2)$, etc.. A similar quantum perturbation theory analysis can be applied to a solid, which gives similar results (see e.g. [15]).

The bound electron nonresonant nonlinear susceptibility of solids can also be understood with the dynamical Franz-Keldysh effect (DFKE) [5, 6], which extends Keldysh's theory of photoionization (where real carriers are created) [17] to the situation where high intensity electric fields modify the band structure of solids via virtual transitions. Qualitatively, an intense EM wave modifies the electron wavefunctions and the overall density of states, causing a blue-shift of the band gap absorption edge on the order of its ponderomotive energy

$$U_p = \frac{2\pi e^2}{mc}\frac{I}{\omega^2} \tag{5}$$

as well as the appearance of an absorption tail to energies below the zero-field band gap (Fig. 1). Absorption and refraction are fundamentally linked through the complex dielectric constant, so any change in absorption gives a corresponding change in refraction. In the low frequency limit, this manifests as a small intensity dependant correction to the refractive index, which can thus be described as $n_{2,\text{eff}}$ and related to a $\chi^{(3)}$ susceptibility.
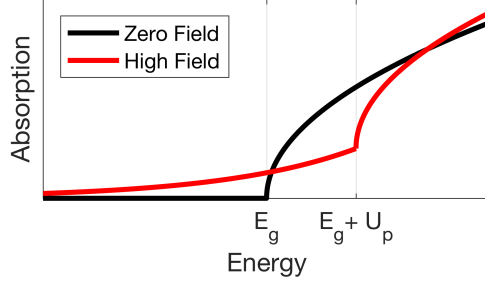
Figure 1: Cartoon displaying the qualitative results of the DFKE. The unperturbed zero field case has absorption profile typical of a density of states with square root dependence on energy. When perturbed with a laser with ponderomotive potential U_p, the absorption edge is blue-shifted, oscillations occur above the band, and a low energy tail forms. This tail is responsible for nonresonant changes to refraction.

2.2   Electronic Band Structure of Solids

Before discussing the free electron contribution to the optical nonlinearity, a brief introduction to the band structure of semiconductors is warranted. In a crystal, an electron wavefunction must obey the periodic boundary conditions imposed by the lattice. Electrons can be described by Bloch functions $\psi_{\vec{k}}(\vec{r}) = u_{\vec{k}}(\vec{r})\exp(-i\vec{k}\cdot\vec{r})$ where $u_{\vec{k}}(\vec{r})$ is a periodic function $u_{\vec{k}}(\vec{r}) = u_{\vec{k}}(\vec{r} + \vec{R})$ and $\vec{k}$ is the wavefunction's wavevector related to momentum using the relationship $\vec{p} = \hbar\vec{k}$. In this way, electron wavefunctions in a lattice can be thought of as plane waves (characteristic of a free particle) with a periodic modulation imposed by the lattice. Fourier transforming the lattice in real space gives a lattice in reciprocal $(\vec{k})$ space with related periodicity. This dual periodicity allows all carrier momenta to be mapped into the first BZ, simplifying analytics and numerics.

In many-particle systems individual wavefunctions overlap and linear combinations of their orbitals can be made to satisfy Schrödinger's equation. In an H_2 molecule for example, the two electrons mix to form a bonding state with negative energy and an anti-bonding state with positive energy. In the solid-state, this is taken to the extreme with $\sim 10^{23}$ particles. *Many* wavefunctions mix together, and discrete energy levels smear, becoming continuous. Similar to bonding and anti-bonding orbitals with an energy gap between, solid-
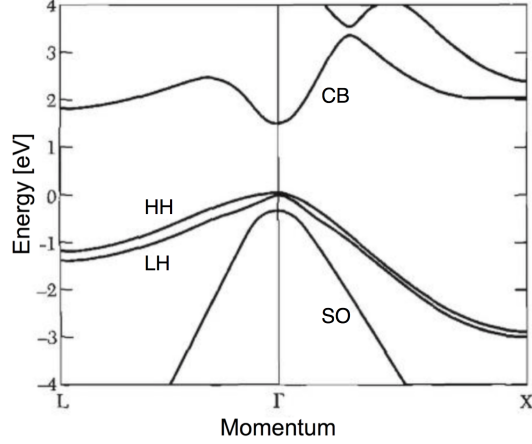
Figure 2: Energy band diagram for GaAs. Important bands are labeled. CB: Conduction band. HH: Heavy-hole band. LH: Light-hole band. SO: Split-off band. Adapted from [18].

state systems will have gaps in their energy density of states, the band gap. The lower energy (filled) valence bands and higher energy (empty) conduction bands are segregated in energy by the Fermi level E_F, which determines the occupation of electrons in the bands.

The three dimensional electronic structure of a solid is typically represented in two dimensional band diagrams, which show the energy dispersion of the bands as a function of momentum $\vec{k}$ in different directions of high symmetry. An example is shown in Fig. 2, where several bands in GaAs are plotted along both the $(k_x, k_y, k_z) = (1, 1, 1)$ and (1,0,0) or L and X directions.

Charge carriers in the conduction and valence bands (electrons and holes, respectively) exist either through injection, thermal generation, photogeneration, or doping. They may take the form of wavepackets with finite position and momentum uncertainty and can be treated with Newtonian mechanics if given an effective mass, m^*. This effective mass is used to compensate for strong static fields inside the crystal. The effective mass of free carriers is found by the curvature of their respective bands

$$\frac{1}{m^*} = \frac{1}{\hbar^2} \frac{\partial^2 E}{\partial k^2}. \tag{6}$$

The negative mass of holes is a sign convention that accounts for their positive charge. The group velocity of an electron wavepacket with central wavenumber $\vec{k}$ can also be accessed by

7

the band structure via

$$v_g = \frac{1}{\hbar} \frac{\partial E}{\partial k}.$$ (7)

When precision is not required, or electrons (holes) possess very little momentum, they remain at the bottom (top) of the conduction (valence) band. At these points, the band dispersion may be represented by a parabola with a constant effective mass — typical values in semiconductors are $m_e^* = 0.1m$ and $m_h^* = 0.5m$

2.3 Free Carrier Nonlinearities

When carriers exist in a semiconductor they interact with the laser fields as free particles would with effective masses as described above. Free carriers can typically be characterized with three timescales, a long interband carrier lifetime τ_R (ns $\to$ μs), an intraband thermalization time τ_T, usually from 1-100 ps, and a short dephasing time T_2, the phase coherence lifetime of interacting dipoles usually between 1 fs and 1 ps. A variety of effects may occur which result in effective $\chi^{(3)}$ nonlinearities, some of which are described here, but generally boil down to carrier populations being transferred to nonequilibrium states where the crystal band structure causes those carriers' contribution to the optical susceptibility to change.

The first of these is free carrier absorption. In equilibrium, the Fermionic nature of electrons forces the carriers to obey Fermi-Dirac statistics. However below carrier concentrations at which the semiconductor is considered degenerate ($N \geq 10^{20}$ cm^{-3}), carrier distributions are well approximated by a Boltzmann distribution. In this way, the carriers can be considered analogous to a classical plasma (where free carriers can be electrons, holes, or both, depending on how the plasma was formed). Using the notation of [19], the dielectric constant takes its usual form

$$\epsilon = 1 - \frac{\omega_p^2}{\omega^2 + i\Gamma\omega}$$ (8)

where

$$\omega_p^2 = \frac{Ne^2}{m^*\epsilon_0}$$ (9)

is the plasma frequency of a carrier with effective mass m^* and Γ is some line broadening

caused by scattering/dephasing processes. If carriers are photoexcited (the situation of greatest interest in this thesis), an average carrier density is

$$N = \frac{I}{\hbar\omega}\alpha\tau_R \tag{10}$$

where α is an effective absorption coefficient generating carriers. Combining these expressions and assuming $\omega \gg \Gamma$ and one carrier with smaller mass than other carriers (usually electrons), n_2 is

$$n_2 = \frac{e^2\alpha\tau_R}{2\epsilon_0\hbar\omega^3 m^* n_0} \tag{11}$$

This result is derived assuming parabolic bands, which is a good assumption for an equilibrium case once the carrier distribution has thermalized.

Despite parabolic bands being useful in many situations, the approximation breaks down when either an appreciable amount of equilibrium carriers are present away from the Γ point or strong electric fields drive carriers away from Γ to regions of the BZ where bands are nonparabolic and effective mass is a function of $\vec{k}$. In this situation there is a nonlinear relationship between momentum and velocity, and thus a nonlinear relationship between momentum and current density $\vec{J} = Nq\vec{v}$. In the classical electromagnetic picture, current density ($\vec{J} = \dot{\vec{P}}$) also acts as a source to the driven wave equation (Eq. 3). This nonparabolicity effect was first observed and described in Refs. [4, 20].

The light emitted by currents can be calculated semi-classically in a single particle model where the particle is accelerated through the bands by the electric field

$$\hbar\frac{d\vec{k}}{dt} = q\vec{E}, \tag{12}$$

an expression which can be integrated over the temporal profile of the pulse to yield $k(t)$. This allows for the calculation of $v_g(t)$ (and thus $J(t)$) in the context of the band dispersion via Eq. 7. The emission is proportional to the Fourier transform of the derivative of the current. Currents radiate with the same parity as $\vec{E}$ due to the symmetry of $\vec{k}$ space in a single direction about Γ - thus nonlinear currents appear as an effective $\chi^{(3)}$ nonlinearity.

In a real semiconductor system, carriers may interact with particles as well as with the field of the laser. Scattering processes occur between carriers and other carriers, phonons,

and, in doped samples, charged impurities - these all act to thermalize carrier distributions. Without concerning too much with the time-dependant perturbation theory derivation of these scattering processes, it is possible to say that at room temperature, carrier-carrier scattering dominates at high excitation/doping densities and may reach rates of 10^{13} s^{-1} at 10^{16} cm^{-3} densities. For densities below this, phonon scattering dominates — e.g. longitudinal optical (LO) phonon scattering in GaAs has rates on the order of 10^{12}-10^{13} s^{-1} for carrier energies above $\hbar\omega_{LO}$ (36 meV). Since phonons carry both energy and momentum they can be involved in 3-body (carrier, phonon, photon) absorption processes, carrier thermalization, as well as intervalley scattering, where carriers in the Γ valley are transferred to secondary valleys with different effective masses that may exist at the edge of the BZ.

2.4 Four-wave mixing

The nonlinear optical process we study in this thesis is nondegenerate collinear four-wave mixing (FWM). FWM is a $\chi^{(3)}$ nonlinear optical effect in which a beam containing two frequencies $\omega_1 < \omega_2$ mix and create a Stokes (low frequency) sideband at $\omega_3 = 2\omega_1 - \omega_2$ and an anti-Stokes (high frequency) sideband at $\omega_4 = 2\omega_2 - \omega_1$ as shown in Fig. 3. In total, 3 photons annihilate to create a single frequency shifted photon. In general, once these first sidebands are created, they mix with the pump frequencies to create a whole family of Stokes and anti-Stokes sidebands all separated by the beat frequency $\Delta\omega$. The experiments in this thesis are all highly nonresonant and thus see rather small dispersion in their linear refractive index. Because of this, and the spectral proximity of the pump frequencies, FWM has a very long coherence length and phase matching will not play a role.
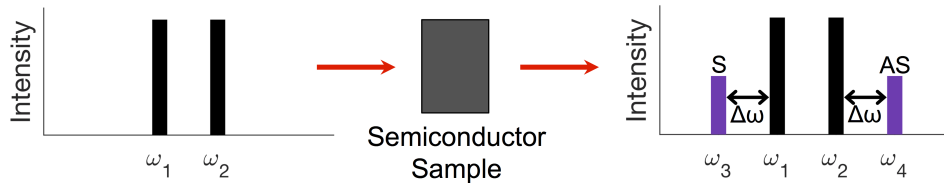
Figure 3: FWM schematic, where S is Stokes and AS is anti-Stokes sidebands.

FWM sideband efficiency (e.g. of the Stokes sideband at ω_3) can be related to $n_{2,\text{eff}}$ analytically in the low efficiency limit. By applying the paraxial approximation ($\partial_z^2 \gg \nabla_\perp^2$), the wave equation driven by a nonlinear polarization $\vec{P}_{NL}$ looks like

$$-\frac{\partial^2}{\partial z^2}\vec{\mathscr{E}}_3 + \frac{n_0^2}{c^2}\frac{\partial^2}{\partial t^2}\vec{\mathscr{E}}_3 = -\frac{1}{\epsilon_0 c^2}\frac{\partial^2}{\partial t^2}\vec{P}_{NL}, \tag{13}$$

assuming a sideband electric field of

$$\vec{\mathscr{E}}_3 = \frac{1}{2}\left[\vec{E}_3 e^{-i(\omega_3 t - k_3 z)} + c.c.\right]. \tag{14}$$

Plugging this electric field into Eq. 13 and applying the slowly varying envelope approximation ($\partial_z^2\vec{E}_3 \ll \partial_z\vec{E}_3$) gives

$$\frac{\partial\vec{E}_3}{\partial z} = \frac{i\omega_3^2}{2\epsilon_0 c^2 k_3}\vec{P}_{NL}e^{i(\omega_3 t - k_3 z)}e^{\alpha_3/2}. \tag{15}$$

where α_j is the absorption coefficient at ω_j. The nonlinear polarization related to the first Stokes FWM sideband,

$$\vec{P}^{(3)} = \frac{3}{4}\epsilon_0\chi^{(3)}(\omega_3 = 2\omega_1 + \omega_2)\vec{E}_1^2\vec{E}_2^* e^{i(\omega_3 t - (2k_1 - k_2)z)}e^{-\alpha_1 - \alpha_2/2}, \tag{16}$$

is inserted into Eq. 15. Without pump depletion, integrating over the length of the crystal L and using Eq. 4 yields

$$I_3 = k_3^2 n_{2,\text{eff}}^2 I_1^2 I_2\left[\frac{e^{-2\Delta\alpha L} - 2\cos\Delta k L e^{-\Delta\alpha L} + 1}{\Delta k^2 + \Delta\alpha^2}e^{-\alpha_3 L}\right] \tag{17}$$

where $\Delta k = 2k_1 - k_2 - k_3$ and $\Delta\alpha = \alpha_1 + \alpha_2/2 - \alpha_3/2$, and the intensity I is defined as

$$I = \frac{cn\epsilon_0}{2}|E|^2. \tag{18}$$

In the simple case where loss is negligible ($\alpha_1 = \alpha_2 = \alpha_3 = 0$), this reduces to

$$I_3 = k_3^2 n_2^2 L^2 I_1^2 I_2 \operatorname{sinc}^2\left(\frac{\Delta k L}{2}\right). \tag{19}$$

In terms of energy W, the experimental observable, the Stokes sideband yield for a phase matched process ($\Delta k L \to 0$) is

$$W_3 = \frac{n_2^2 L^2 k_3^2}{\sqrt{3}\tau^2 A^2}W_1^2 W_2 \tag{20}$$

where τ is the pulse length, A is the beam area, and the $\sqrt{3}$ factor arises due to a shortening of the sideband pulse length in the low conversion efficiency regime [21].

11

3 Experimental Setup

Four-wave mixing experiments in semiconductors were performed using a 1 Hz high-power CO_2 laser system. There were two different intensity regimes used in the experiments, a low intensity regime from 1-10 MW/cm^2 ($\tau = 300$ ns) and a high intensity regime from 1-10 GW/cm^2 ($\tau = 200$ ps). For both sets of experiments, the master oscillator was a transversely excited atmospheric (TEA) CO_2 laser with two low pressure (narrow linewidth) CO_2 amplifiers in the cavity coupled together with an intracavity grating, allowing simultaneous oscillation on two frequencies. The majority of experiments in this thesis used a beat-wave of the 10P(20) ($\lambda = 10.59\mu$m) and 10R(16) ($\lambda = 10.27\mu$m) rotational lines of the CO_2 molecule giving a beat frequency $\Delta f = 872$ GHz.

This laser produced a typical temporal profile shown in Fig. 4(a). As nonlinear interactions depend strongly on intensity, the μs tail of the pulse participates very little in nonlinear optics. Instead, only the first gain switched spike of the pulse is considered, which is found to fit a Gaussian profile with FWHM 300 ± 10 ns. This 300 ns beat-wave had a nominal
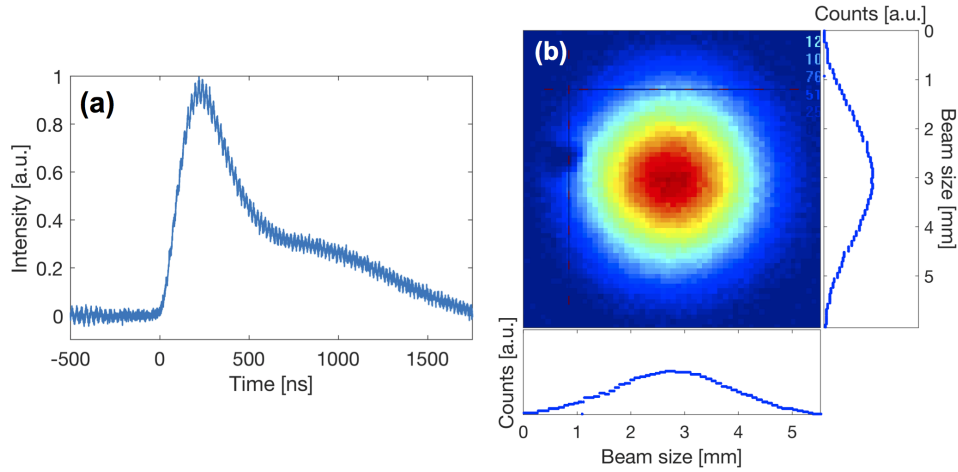
Figure 4: (a) Temporal pulse profile of the TEA CO_2 laser. (b) Beam profile of the 300 ns CO_2 laser pulse at the interaction point. Lineouts are taken at the center of the beam (blue points). Gaussian fitting is performed (not shown). The hole in the left side of the image is a burned region on the pyroelectric chip.

energy of 25 mJ at $\lambda = 10.59\mu$m and half that energy at $\lambda = 10.27\mu$m, with very little fluctuation from shot to shot ($\pm 5\%$). The difference in gain coefficients on the 10P and 10R branches of the CO_2 gain spectrum caused the measured difference in energy between the two wavelengths. Laser intensity on the sample was controlled by lowering the TEA CO_2 laser's discharge voltage or placing CaF_2 attenuators in front of the sample. Calibrations for these attenuators are given in Appendix A.

This laser pulse was used for the low intensity measurements (Fig. 5). The beam was focused using a 2.5 m focal length curved copper mirror creating a slightly elliptical spot at the focus, which was measured using a pyroelectric camera. The major and minor axes had FWHM of 2.81 and 2.55 mm respectively (Fig. 4(b)). The beam area could be approximated as a circle with FWHM of 2.68 ± 0.03 mm with less than 1% error. Samples were placed just beyond the focus to help compensate for self-focusing. The Rayleigh length was >50 cm, several times longer than any of the samples so that the beam inside the sample could be considered a plane wave. To increase the effective nonlinear length of the samples, the beam was sent through a zig-zag arrangement as shown and samples were placed on a translational stage which could be moved such that there were 1, 2, or 3 passes through the sample.
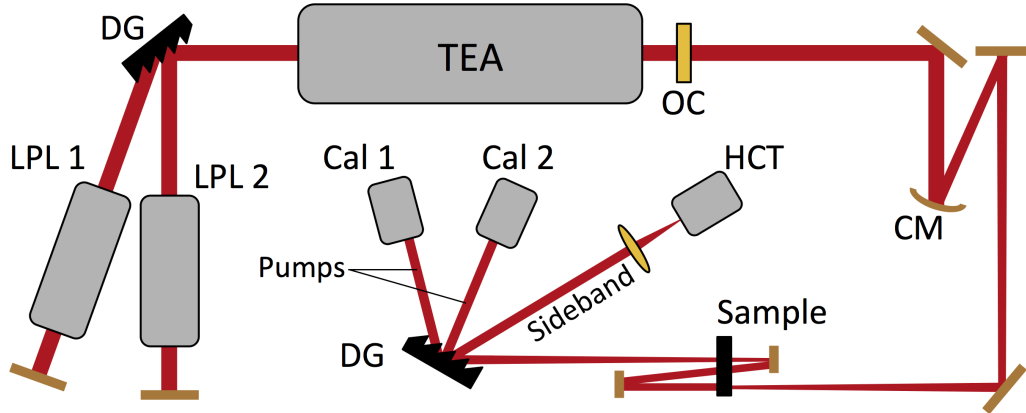
Figure 5: Schematic of the experimental setup to measure FWM sidebands at intensities from 1-10 MW/cm^2. DG is diffraction grating, OC is output coupler, CM is the 2.5 m focal length curved copper mirror, Cal is calorimeter, and HCT is HgCdTe energy detector.

After the sample, the beam was dispersed by a reflective diffraction grating with 135 grooves/mm and reflectivity >97% in the spectral range of interest. The Stokes sideband at $\lambda = 10.93\mu$m was focused by a 1 inch focal length ZnSe lens onto the 1 mm x 1 mm chip of a liquid nitrogen cooled HgCdTe (HCT) energy detector with spectrally flat sensitivity from 10-11 μm. Pump beam energies were measured on every shot with large aperture calorimeters.

To generate high intensity pulses, the 300 ns 10 μm pulse was combined with a 200 ps 1.064 μm Nd:YAG laser pulse in a CS_2 cell (Fig. 6). The 1 μm pulse induced transient birefringence in CS_2 via the optical Kerr effect, rotating the polarization of the 10 μm pulse only while the two beams overlapped [22]. After an analyzer only the 200 ps 10 μm pulse remained, containing nJ of energy. This short two-wavelength pulse was amplified by an 8 atm CO_2 regenerative amplifier and a 10 atm CO_2 booster amplifier to return it to the mJ level. A CdTe Pockels cell selected the most intense pulse in the pulse train exiting the regenerative amplifier. At this point a small reflection from a NaCl window was dispersed
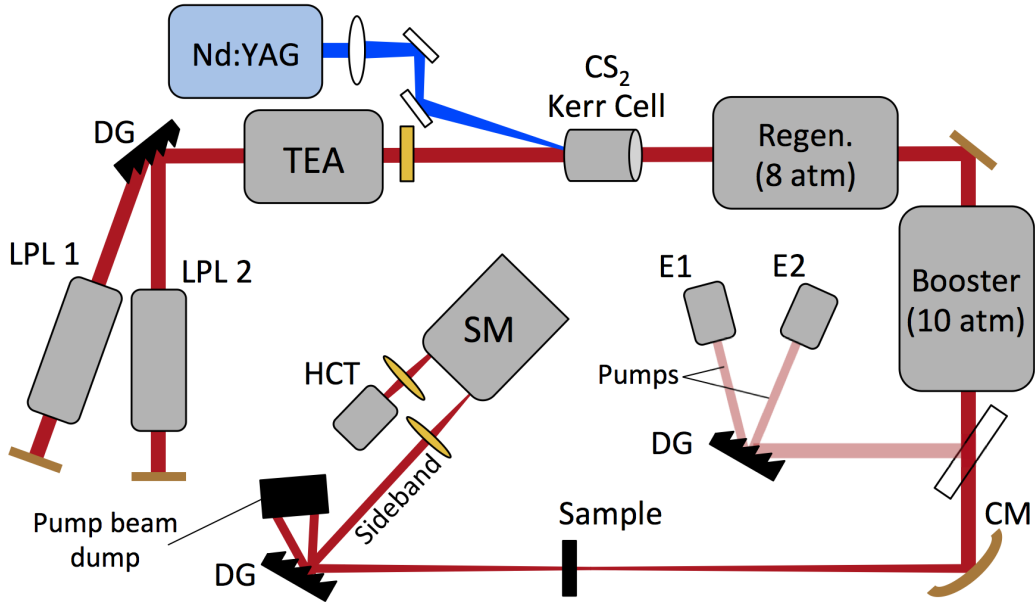
Figure 6: Schematic of the experimental setup to measure FWM sidebands at intensities from 1-10 GW/cm^2. E1 and E2 are energy meters and SM is the scanning monochomator.

14
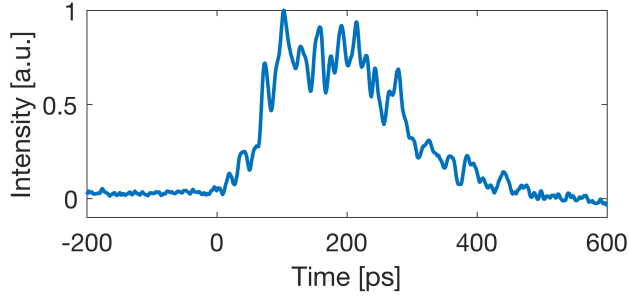
Figure 7: Temporal pulse profile of the CO_2 laser beat-wave measured to be 200 ± 20 ps.

and the total energy in each pump wavelength was measured by energy meters on every shot and used for normalization of the sideband energy. The temporal pulse profile was measured with a streak camera to have a FWHM of 200 ± 20 ps (Fig. 7).

The 200 ps pulse was focused by a 2.5 m focal length curved copper mirror to a slightly elliptical spot. A FWHM spot size of 820 ± 20 μm on the surface of the GaAs and Ge samples was measured using the same circular approximation (Fig. 8(a)). Due to the mount and space restrictions, the position of the ZnSe crystal was slightly in front of the GaAs and Ge position and had a slightly smaller FWHM spot size of 790 ± 50 μm (Fig. 8(b)).

The Rayleigh length was on the order of 20 cm, so inside the crystals the plane wave approximation still held. CaF_2 attenuators were placed either after the regenerative amplifier or in front of the HCT detector to coarsely control the intensity on the crystal samples. Each pump beam contained nominally 0.5-5 mJ, with similar difference between pumps as in the low intensity measurements. Intensity scatter was inherent in these measurements, as small intensity fluctuations grew along the chain of amplifiers.

The beam was dispersed by the same 135 groove/mm grating and pump frequencies were dumped on a razor-blade stack. The sideband was focused with a short focal length ZnSe lens onto the 2mm wide input slit of a scanning monochromator (Horiba Jobin Yvon iHR-550) loaded with a 50 groove/mm grating blazed at 12 μm. This spectrometer could be tuned across the entire range of sideband wavelengths used in experiments. After the 0.5mm output slit, a short focal length ZnSe lens focused the beam onto the same cryogenically cooled HCT energy detector.

15
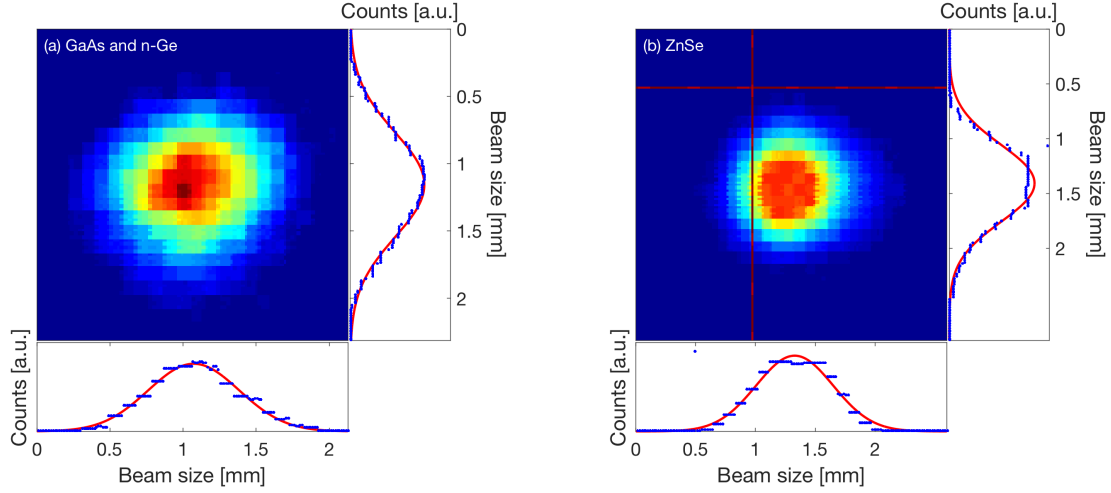
Figure 8: Beam profile of the 200 ps CO_2 laser pulse measured with a pyroelectric camera at the interaction point for (a) GaAs and n-Ge and (b) ZnSe.

Several samples were used in FWM experiments:

- 7 mm thick anti-reflection (AR) coated semi-insulating GaAs slab with resistivity $>$ $3 \times 10^8 \, \Omega \cdot$cm. Measurements were performed with the electric field parallel to the [111] axis. $E_g = 1.42$ eV (direct).

- 700 μm thick semi-insulating (110) GaAs wafer with resistivity between 1 and 4 $\times 10^8 \Omega \cdot$cm. Rotating the crystal about the (110) axis allows for a normally incident linearly polarized beam to be parallel to the orientations $[001], [1\bar{1}1], [1\bar{1}0]$, equivalent in the zincblende crystal structure to the [100], [111], and [110] orientations, respectively. $E_g = 1.42$ eV (direct).

- 2 mm and 3mm thick n-type Ge slabs of optical quality (carrier concentration not known exactly, but optical grade Ge typically has Sb doping of $\sim 10^{14}$ cm^{-3} and resistivity $\sim 10 \, \Omega \cdot$cm [23, 24]). $E_g = 0.66$ eV (indirect).

- 5 mm thick polycrystalline ZnSe slab. $E_g = 2.71$ eV (direct).

- 12 mm thick polycrystalline ZnSe slab. $E_g = 2.71$ eV (direct). Grain size has been

16

estimated to be 43 ± 15 μm for both ZnSe samples (See Appendix B.)

All band gaps stated are room temperature values. We also attempted to measure FWM in a 3 cm thick CdTe sample ($E_g = 1.44$ eV), however the signal was immeasurably small and plasma could occasionally be seen forming on the entrance surface of the crystal. Breakdown at or near the surface of the crystal likely absorbed enough pump photons to render the nonlinear interaction in the bulk negligible.

Many of the measurements in this thesis focused on the 1st Stokes FWM sideband. Pump energies and sideband energy were measured on every shot so that they could be normalized to each other. Data sets consisted of 60-100 shots, half with the sample in the beam path and half with the sample removed from the beam path (background). The background originated either from scattered light or four-wave mixing in the many windows, polarizers, and other optical elements in the between the master oscillator and detector, as well as in the air. In order to eliminate background signal and improve the signal to noise ratio (S/N) of the high intensity measurements, a 700 μm thick (100) GaAs wafer was placed $\sim$1m before the sample, which selectively reflected certain frequencies depending on the beam's angle of incidence. Fig. 9 shows transmission curves. Empirically, tuning the etalon to 11.5° allowed for an improved S/N for the HFBW measurements. Additionally, the grating between the sample and spectrometer acted as a power filter to increase the S/N.
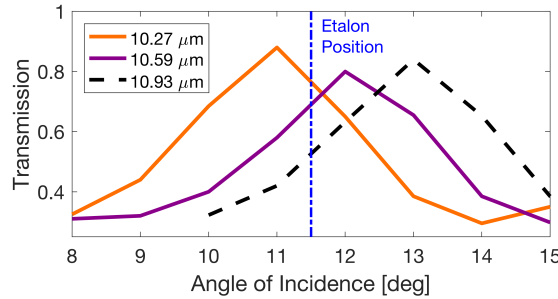
Figure 9: Transmission through a 700μm thick (100) GaAs wafer. Solid lines are measured in Ref. [25] and the dashed line is an extrapolation of that measured data.

17

4   Four-Wave Mixing Efficiency and $n_{2,\text{eff}}$ Measurements

Four-wave mixing was performed in the semiconductors GaAs, n-Ge, and ZnSe with 10.27 μm and 10.59 μm beat-wave radiation from a CO_2 laser. As described above, both a low intensity (long 300 ns pulse) and a high intensity (short 200 ps pulse) regime were studied in each of the three materials with the intention of measuring the effective nonlinear refractive index via Eq. 17.

An example of the low intensity raw data is shown in Fig. 10. The measured first Stokes sideband energy W_3 at $\lambda_3 = 10.93$ μm is plotted against $W_1^2 W_2$ which should give a linear slope to the data. Indeed for the data taken with the sample in the beam-path the linear fitting works rather well. However the background data does not fit well with a linear slope and instead takes on the shape of a power function of the form ax^b. This power fitting is a clear indication that the background is dominated by scattered light as opposed to FWM light generated in previous optical elements.
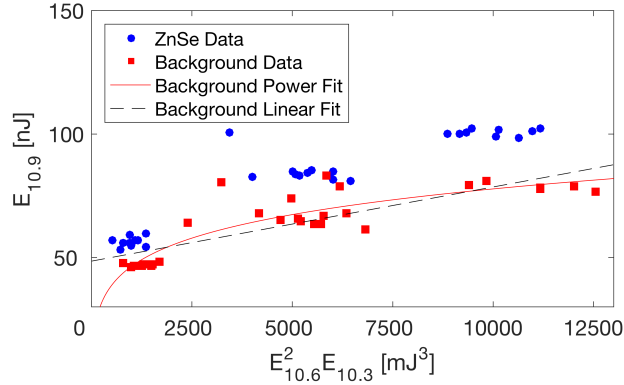
Figure 10: Example of raw FWM data measured in polycrystalline ZnSe around 4 MW/cm^2, showing "sample in" and background "sample out" measurements of the 1st Stokes sideband at 10.93 μm. The fact that the power curve fits the background data better indicates that scattered light dominates the measurement.

Data points being grouped together is a consequence of the way the intensity scan was performed. Each group represents a different level of attenuation, with the lower energy points from either 2 or 3 mm of CaF_2 being placed in front of the sample (or in some cases,

18

the voltage on the TEA CO_2 discharge being lowered). Specifically for the low intensity case the samples used are the 7mm [111] GaAs slab at normal incidence, the 2mm and 3mm n-Ge slabs with light incident at Brewster's angle, as well as the 5 mm ZnSe window at normal incidence. For GaAs and ZnSe, only the 2 and 3 pass measurements produced significant FWM signal above background, and are the only measurements considered at low intensity for these materials. For all the low intensity measurements the loss in the samples was negligible and the interaction is well phase-matched over the length of the crystals, so Eq. 20 is valid.

In order to make an $n_{2,\text{eff}}$ measurement, the background fit was subtracted from each data point. Each individual point was plugged into Eq. 20 to calculate the distribution of $n_{2,\text{eff}}$ values over many shots. Histograms of these distributions are presented in Fig. 11, where the mean is indicated by the red dashed line. For most data sets, the lowest intensity grouping was strongly affected by noise and gave artificially large values of $n_{2,\text{eff}}$; these data were removed from this analysis. Uncertainty in these measurements is dominated by scattering in the value of $n_{2,\text{eff}}$, as the relative uncertainty in the other parameters (beam size, pulse length) are rather small.

The 2mm and 3mm long n-Ge samples that were measured gave slightly different results, as shown by the different colored data in Fig. 11. $n_{2,\text{eff}}$ in the 2mm sample was found to be $64 \pm 17 \times 10^{-14}$ cm^2/W, whereas it was measured as $105 \pm 15 \times 10^{-14}$ cm^2/W in the 3mm
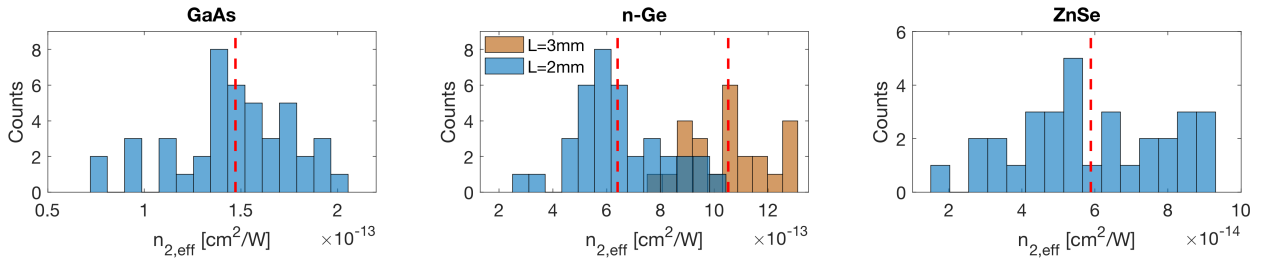
Figure 11: Distribution of $n_{2,\text{eff}}$ measured for GaAs, n-Ge, and ZnSe at 1-10 MW/cm^2. The means are indicated by the vertical red lines. The two n-Ge samples were measured to have different $n_{2,\text{eff}}$ distributions as shown.

sample. This difference may arise from a difference in carrier concentration between the two samples, which has been shown to affect the nonlinearity at high enough densities [26].

Both absolute and relative (normalized to GaAs) $n_{2,\text{eff}}$ measurements at low intensity are presented in Table 2, where the average of the n-Ge values is given.

For high intensity, a similar data analysis was performed. As can be seen in the raw data example of Fig. 12, the background data follows the linear dependence, confirming that the majority of the background is FWM light generated in the laser system and transport - the scanning monochromator greatly reduces the scattered light incident on the cryo HCT detector.
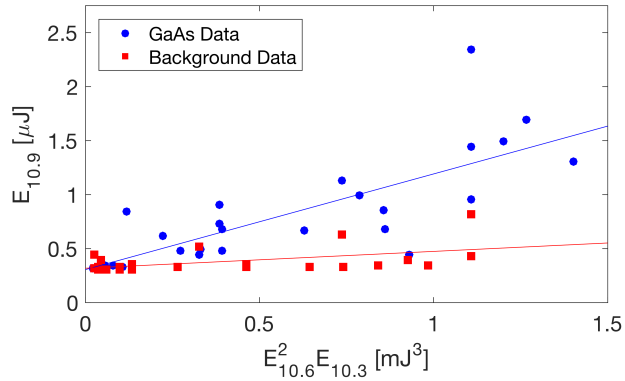
Figure 12: Example of raw FWM data measured in [111] GaAs around 2 GW/cm^2. Data displayed here is the 1st Stokes sideband generated in the 7mm [111] GaAs slab at approximately 2 GW/cm^2.

The samples used in these short pulse measurements were the 7mm [111] GaAs slab, the 2mm n-Ge slab, and the 12mm ZnSe slab. The 5mm ZnSe windows were used, but did not generate sufficient Stokes sideband energy to make a conclusive measurement of $n_{2,\text{eff}}$. The ZnSe sample was measured at normal incidence and the n-Ge sample was measured at both Brewster's angle and normal incidence, so Fresnel reflection of the pump light on the entrance face and of the sideband light on the exit face had to be taken into account.

At intensities > 1 GW/cm^2, it was found that all of the samples had intensity dependant transmission characteristics. Nonlinear absorption in these samples was characterized by using a 200 ps CO_2 laser pulse with a single wavelength of $\lambda = 10.59$ μm and measuring

20
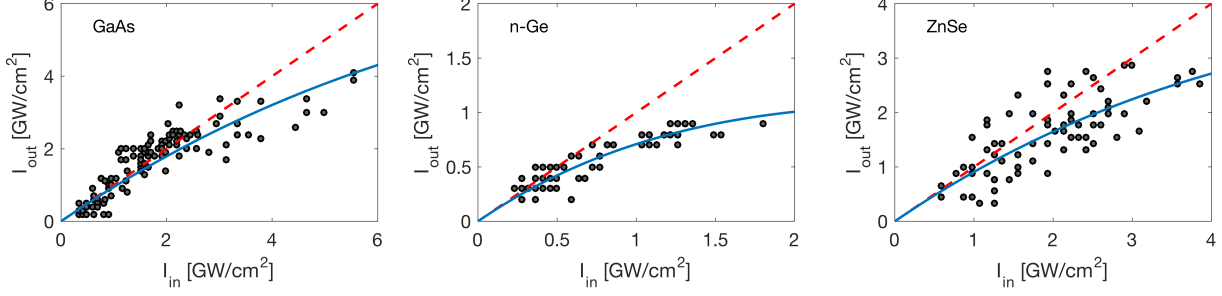
Figure 13: Nonlinear absorption data measured at $\lambda = 10.59$ μm for the semiconductors studied in this thesis. The dashed lines denote lossless propagation and the solid curves denote the fit to the data.

	GaAs	n-Ge	ZnSe
α_{NL} [cm/GW]	0.08 ± 0.02	1.7 ± 0.1	0.08 ± 0.02

Table 1: Nonlinear absorption coefficients measured in semiconductors at 10.59 μm with an effective absorption coefficient of the form $\alpha_{\mathrm{eff}} = \alpha_{\mathrm{NL}} I_{\mathrm{in}}$.

the input and output intensity from each material. This data is given in Fig. 13. For each sample, the red dashed line represents the lossless Fresnel reflection-only transmission and the blue curve is a fit using the equation [24, 27]

$$I_{\mathrm{out}} = I_{\mathrm{in}}\exp\left(-\alpha_{\mathrm{eff}}L\right) \tag{21}$$

where α_{eff} is the effective absorption coefficient; the best fitting form was found to be $\alpha_{\mathrm{eff}} = \alpha_{\mathrm{NL}} I_{\mathrm{in}}$. The values of α_{NL} measured for each sample are displayed in Table 1. Linear absorption for our samples is considered negligible in this analysis.

Nonlinear absorption is an indicator of interaction between the laser field and free carriers, whether in an interband photoionization process, through the driving and relaxing of intraband currents, or free carrier absorption. Photoionization and subsequent free carrier processes are not unexpected in n-Ge, which has a narrow (relative to $\hbar\omega$) direct band gap of 0.8 eV as well as pre-existing free carriers, or in polycrystalline ZnSe in which many crystal

facets and corners could potentially allow for surface effects and local field enhancement to contribute to the generation of free carriers despite the wide 2.71 eV band gap. Free carrier processes in semi-insulating GaAs (specific resistivity $> 3 \times 10^8$ Ω·cm) are more unexpected, as it has a relatively wide band gap at 1.42 eV and is designed to have as few free carriers as possible at equilibrium. Section 5 discusses the case of GaAs in more depth.

The presence of nonlinear absorption requires that the full expression Eq. 17 be used to calculate $n_{2,\text{eff}}$. In the case of the intensity dependant absorption measured above, $\alpha_3 = 0$ and we assume that $\alpha_1 = \alpha_2 = \alpha_{\text{NL}}I$, with I a characteristic intensity for the data, making $\Delta\alpha = 3\alpha_{\text{NL}}I/2$. Using experimental observables, the entire expression simplifies to

$$W_3 = \frac{n_{2,\text{eff}}^2 L^2 k_3^2}{\sqrt{3}\tau^2 A^2} W_1^2 W_2 \left[\frac{1}{L^2} \frac{e^{-3\alpha_{\text{NL}}IL} - 2\cos\left(\Delta k L\right)e^{-\frac{3}{2}\alpha_{\text{NL}}IL}}{\Delta k^2 + \frac{9}{4}\alpha_{\text{NL}}^2 I^2} \right]. \tag{22}$$

Nonlinear absorption will increase $n_{2,\text{eff}}$ by the square root of the inverse of the factor in the square brackets due to dynamic pump absorption over the course of the interaction. This factor is shown for each material in Fig. 14, where it is evident that absorption plays a role even at intensities toward the bottom of the intensity range - the sideband yield and thus nonlinear refractive index in n-Ge is dramatically affected by nonlinear absorption.

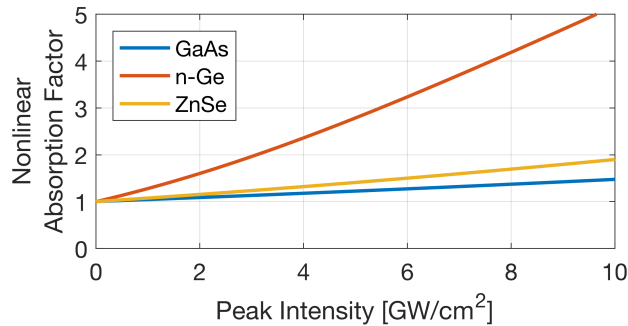Figure 14: Calculated multiplication factor of $n_{2,\text{eff}}$ caused by measured values of nonlinear absorption in our semiconductor samples.

A point by point analysis of $n_{2,\text{eff}}$ in n-Ge (and to a lesser extent GaAs and ZnSe) yielded a downward trend with intensity before the nonlinear absorption was taken into account (simply using Eq. 20). After considering nonlinear absorption, the slope went to zero within
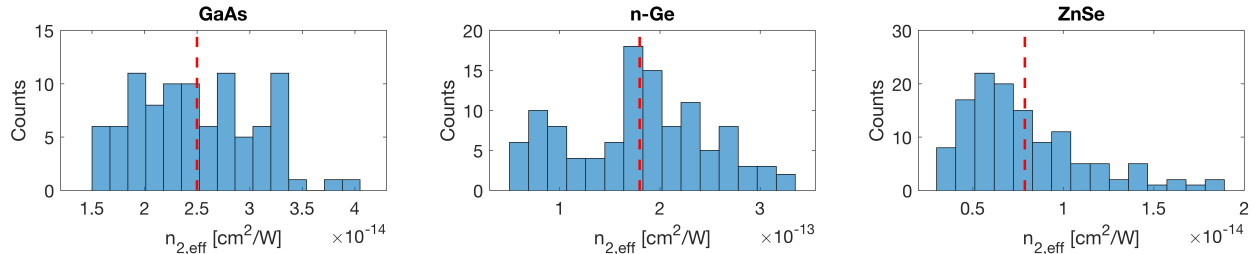
Figure 15: Distribution of $n_{2,\text{eff}}$ measured for GaAs, n-Ge, and ZnSe at 1-10 GW/cm^2. The means are indicated by the vertical red lines.

experimental uncertainty, indicating $n_{2,\text{eff}}$ is constant with input pump intensity.

Measured $n_{2,\text{eff}}$ distributions for each of these materials is shown in Fig. 15, with the values displayed in Table 2. Uncertainty was again dominated by the statistics of the data.

The literature gives a range of $n_{2,\text{eff}}$ values for GaAs at 10 μm. Particularly, in a similar experiment using FWM, Wynne [3] measured a value of $n_{2,\text{eff}} = 4 \pm 2 \times 10^{-14}$ cm^2/W using 1 MW/cm^2 10.6 μm CO$_2$ lasers. Additionally, Hurlbut et al. [29] measure $n_{2,\text{eff}}$ using the Z-scan technique [2] at 1.5-3 μm in the intensity range 3-11 GW/cm^2. These measurements indicate that $n_{2,\text{eff}}$ decreases with wavelength from 30×10^{-14} cm^2/W to 10×10^{-14} cm^2/W, with the dispersion due to a two-photon resonance around 1.7 μm. Extrapolating yields a value of 8×10^{-14} cm^2/W at 10.6 μm.

In n-Ge, $n_{2,\text{eff}}$ has also been found by Wynne to be $30 \pm 15 \times 10^{-14}$ cm^2/W using FWM.

The nonlinear refractive index of ZnSe has been well characterized near resonance in the visible [30], but has been measured nonresonantly only recently by Werner et al. [28] using a Z-scan at 3.9 μm with intensities ranging from 5-20 GW/cm^2. This measurement gives $n_{2,\text{eff}} = 1.2 \pm 0.3 \times 10^{-14}$ cm^2/W and predicts essentially flat dispersion out to longer wavelength.

These literature values are also presented in Table 2. There is some disagreement in the absolute values of $n_{2,\text{eff}}$ measured in this work and those from the literature. Additionally, our measured values of $n_{2,\text{eff}}$ do not agree at high and low intensity irradiation, even for the same samples. Of critical importance, however, is that the relative magnitude of $n_{2,\text{eff}}$ for

23

Intensity	$n_{2,\text{eff}}$ $[10^{-14}$ $cm^2/W]$		
	GaAs	n-Ge	ZnSe
1-10 GW/cm^2	2.5 ± 0.6	18 ± 7	0.8 ± 0.3
1-10 MW/cm^2	15 ± 3	85 ± 20	6 ± 2
Literature	4 ± 2^a	30 ± 15^a	1.2 ± 0.32^b
Intensity	$n_{2,\text{eff}}$ [a.u.]		
1-10 GW/cm^2	1	7 ± 3	0.3 ± 0.15
1-10 MW/cm^2	1	6 ± 2	0.4 ± 0.15
Literature	1	7.5 ± 5	0.3 ± 0.17

Table 2: $n_{2,\text{eff}}$ measured with FWM in semiconductors. The literature values are taken from a: [3] and b: [28]. Both absolute and relative measurements are presented.

both intensity regimes and in the literature are identical within experimental uncertainty.

Since our MW/cm^2 measurements give consistently higher nonlinearity than literature and GW/cm^2 measurements but the same relative ratio among the materials, some systematic error causes an artificially large energy reading for the Stokes sideband. Because these measurements were plagued by scattered light as described above, it is likely that this scattered light systematically increased the signal on our cryo HCT detector in a way that cannot be removed from the data in a simple standardized way.

Our GW/cm^2 measurements give mean $n_{2,\text{eff}}$ consistently slightly lower than the literature, however agree within experimental uncertainty on both absolute and relative scales, likely a result of the scattered light and background being well mitigated by the scanning monochromator and etalon. It is possible that a small amount of pump depletion, which is ignored in the analytic FWM theory, dynamically reduces the sideband yield giving smaller $n_{2,\text{eff}}$. For the sideband yields measured in experiments (on the order of $10^{-4} - 10^{-3}$), this should not play a large role — if similar measurements were performed at higher intensities, the pump depletion would invalidate assumptions made during the derivation of Eq. 17.
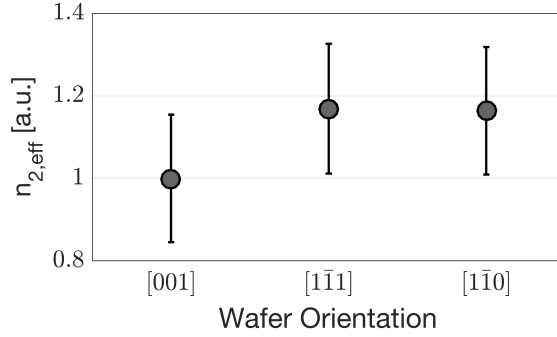
Figure 16: Anisotropy of $n_{2,\text{eff}}$ in a GaAs wafer with the electric field of the laser aligned along different crystal orientations.

Finally, the anisotropy of $n_{2,\text{eff}}$ was measured in the 700μm thick (110) GaAs wafer using 200 ps pulses. As described in Section 3, the (110) surface orientation allows for probing of the three main symmetry directions of the zincblende crystal structure. Figure 16 shows relative $n_{2,\text{eff}}$ extracted for each orientation. Despite relatively large experimental uncertainty, the anisotropy of the mean values of $n_{2,\text{eff}}$ in GaAs follows the same trend found experimentally from 2-3 μm [29] and in calculations for nonresonant interactions [31]. Our measured values also qualitatively follow the trend seen in the second order optical nonlinear susceptibility $(\chi^{(2)})$ of GaAs [32]. This anisotropy arises from stronger dipoles between Ga and As ions existing in the [111] and [110] directions.

5 Control of the Nonlinear Optical Response with the CO$_2$ Laser Beat-Wave

GaAs is widely regarded as a standard material in the study of both nonlinear optics and semiconductor physics due to its robust optical and electrical properties as well as the most developed technology involved in growing impurity free crystals. For these reasons, we study GaAs in more depth both in experiment and with simulations, the results of which are presented in this section.

Specifically, we studied the nonlinear response of [111] GaAs with two different CO$_2$ laser

25

beat-waves — the first the same as used in the measurements in Section 4, with $\lambda_1 = 10.59\mu$m and $\lambda_2 = 10.27\mu$m and $\Delta f = 872$ GHz, which will be called the high frequency beat-wave (HFBW), as well as with a low frequency beat-wave (LFBW) with $\lambda_1 = 10.59\mu$m and $\lambda_2 = 10.27\mu$m (10P(20) and 10P(16) lines of the CO_2 laser) that has $\Delta f = 106$ GHz [33]. The same experimental setup was used as in the previous high intensity FWM measurements with only slight modifications. In particular, to help characterize the nonlinearity in GaAs, we measured a full spectrum of FWM sidebands on both the Stokes and anti-Stokes sides. To achieve the resolution required to measure the spectrally close sidebands of the LFBW, a diffraction grating with 100 grooves/mm blazed at 9 μm was placed inside the spectrometer. Additionally the etalon was removed for LFBW measurements, as it was found to have no beneficial effect in reducing background signal; as a consequence LFBW measurements were performed at higher peak intensities (4-8 GW/cm^2) than the HFBW measurements (1-4 GW/cm^2) and had slightly higher uncertainty from a worse S/N.

To compare these two cases, the power of each FWM sideband was measured and compared to the power in the pump beat-wave. The results of FWM spectrum measurements are displayed in Fig. 17(a) for the HFBW and Fig. 17(b) for the LFBW. The difference between the two beat-waves is striking. The LFBW has much higher efficiency for all sidebands, and more sidebands on both the Stokes and anti-Stokes side were detectable above the background (despite the higher background signal). Taking as an example the Stokes sideband, the sideband yield is 40x higher for the LFBW than for the HFBW. With consideration of the intensity scaling of the yield $I_3/I_1 \propto n_{2,\text{eff}}I_1I_2$, this corresponds to an $n_{2,\text{eff}}$ in GaAs 3.3x larger when using a 106 GHz beat-wave instead of a 872 GHz beat-wave. For the many nonlinear optical processes which sensitively depend on $n_{2,\text{eff}}$ (or equivalently $\chi^{(3)}$), including FWM and SPM, the power requirements to observe nonlinear effects can be dramatically reduced. As a consequence, these nonlinear optical processes may be more useful in technological applications where high power lasers may not be available, practical, or integrable.

To determine the cause of the beat-wave enhancement of the nonlinearity, we look back to
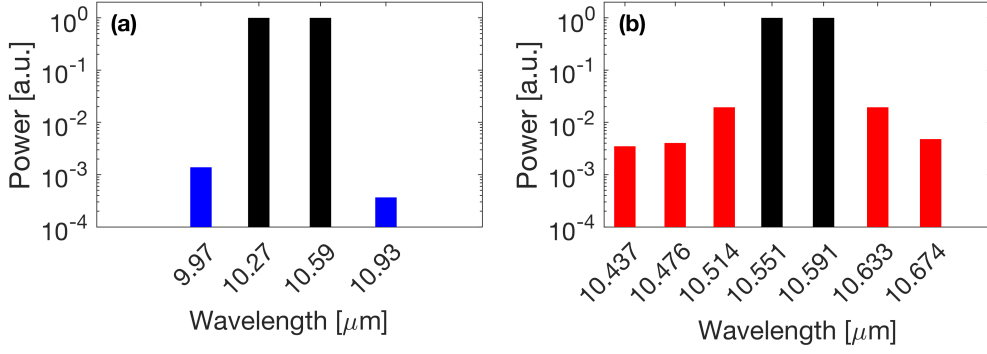
Figure 17: Full FWM spectrum measured in GaAs using the (a) HFBW and the (b) LFBW.

the nonlinear absorption in our 7mm [111] GaAs as shown in Fig. 13. This is an interesting observation in GaAs with both a relatively wide band gap (compared to the photon energy, $E_g \approx \hbar\omega/12$) and a lack of free carriers existing at room temperature thermal equilibrium - a simple estimate yields a carrier concentration of 10^6 cm^{-3} at the bottom of the conduction band. Using free carrier absorption theory (Eq. 8-11) with the effective absorption coefficient $\alpha_{NL}I$ as measured in GaAs, a very high average carrier concentration of $\sim 10^{20}$ cm^{-3} is found. A 1 ns interband recombination time is assumed [34]. Using the same assumptions in Eq. 11, a massive n_2 of 5×10^{-9} cm^2/W is found, orders of magnitude larger than that measured in experiment - pure free carrier absorption cannot explain the nonlinearity in GaAs.

In order to more accurately characterize the free carrier dynamics we use Keldysh's theory of ionization [17], which denotes three different regimes of ionization, delineated by the Keldysh parameter $\gamma \propto \sqrt{E_g/U_p}$. $\gamma \gg 1$ is the multiphoton ionization regime, where the standard picture of photon stacking applies. $\gamma \ll 1$ is the tunneling regime, where the band gap is modified, allowing for tunneling. When $\gamma \approx 1$, these processes merge, and nonperturbative processes can be observed. The high intensities in our experiments combined with the large ponderomotive energy ($I\lambda^2$ scaling), makes $\gamma = 1$-2 for our measurements. Fig. 18 shows both the Keldysh ionization rate in GaAs as well as an estimate of the free carrier concentration found by integrating the ionization rate over the intense 200 ps long beat-wave (it does not change with Δf - it is purely a field effect). Qualitatively, Keldysh's theory
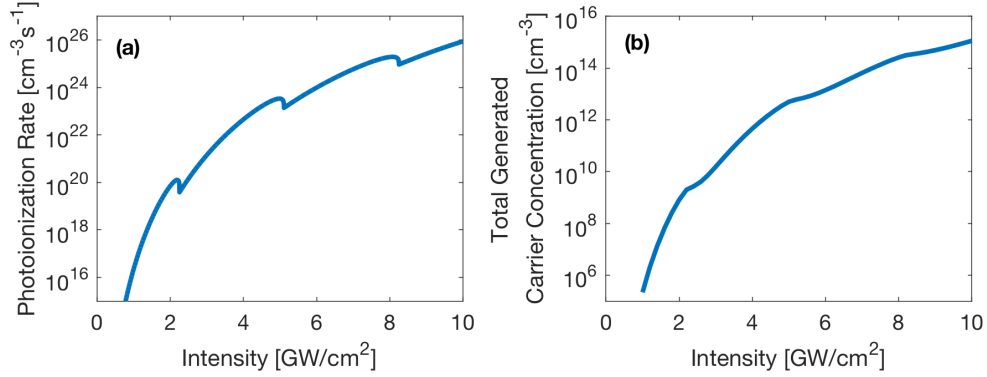
Figure 18: (a) Photoionization rate for GaAs and (b) Carrier concentration generated in GaAs for the CO_2 laser HFBW of varying peak intensity calculated using Keldysh's theory [17].

shows that a significant number of nonequilibrium free carriers can be produced during our laser-semiconductor interaction.

Using the semi-classical theory based off Eq. 12, it is found that peak beat-wave intensities used in experiments can drive nonequilibrium electrons to states with non-negligible k values such that the parabolic approximation is no longer valid (holes are driven by the field as well, but their larger mass keeps them more localized at the top of the valence band). In these high fields, electrons rather easily achieve energies greater than the LO phonon energy (36 meV). These hot carriers emit LO phonons or scatter between CB valleys on τ_T timescales. Over the course of the 200 ps long pulse, many cycles of carrier excitation and relaxation/dephasing occur, contributing to nonlinear absorption of the laser beam. Due to these complicated nonparabolic and hot carrier effects, the semiconductor Bloch equations (SBEs) ([35, 36]) were used to model the nonlinear response of GaAs. The SBEs self-consistently model the light-semiconductor interaction such that all orders of the nonlinear optical susceptibility are included.

The band structure of [111] GaAs was calculated using density functional theory (DFT), giving the band structure in Fig. 19, showing the 4 major bands near the Fermi level: conduction band (CB), heavy-hole (HH), light hole (LH), and split-off (SO) valence bands. DFT also gives dipole moments between each band across all k-space. It is found that when
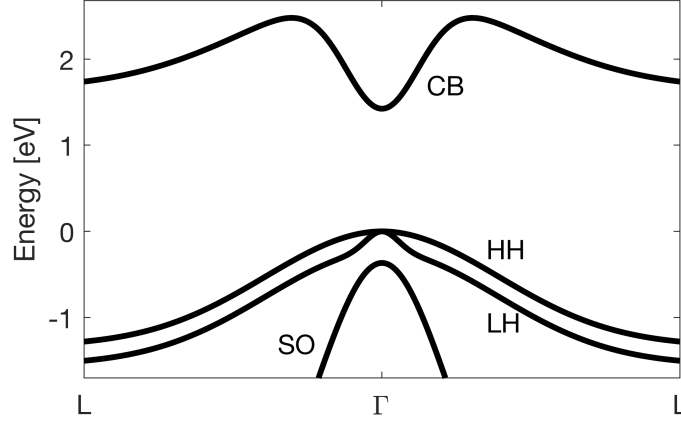
Figure 19: Electronic band structure of GaAs in the [111] direction calculated with DFT.

$\vec{E}$ ‖[111], the HH-CB dipole moment vanishes. A much stronger dipole exists between LH-CB than SO-CB, causing the SO dynamics to be rather inconsequential to the nonlinear response of GaAs; simulations are performed using a 2-band model including the CB and LH bands.

To compare simulation results with experiment, the 1st Stokes FWM sideband efficiency is calculated as a function of peak input intensity using both the HFBW and LFBW. The ratio of pump intensities is taken to be $I_1/I_2 = 2$, modeled after experiment. GaAs is assumed to be initially unexcited, and a polarization dephasing time $T_2 = 300$ fs is used. T_2 automatically takes into consideration Coulombic mean field interactions and various scattering processes. In the SBEs there is an interband polarization response as well as an intraband current response in the material. Both of these act as sources of radiation modulated at Δf, producing FWM sidebands. Results of these simulations are the solid lines in Fig. 20, blue for the HFBW and red for the LFBW, which show the same beat-wave enhancement as experiment. These curves are smoothed over oscillations with intensity which are attributed to Rabi flopping of the carrier concentrations and polarizations. Experimental sideband efficiency is overlaid as dots of corresponding color, which matches the simulations with reasonable agreement. Uncertainty in efficiency and intensity are calculated from the scatter of the data, and the experimental resolution was not high enough to observe any
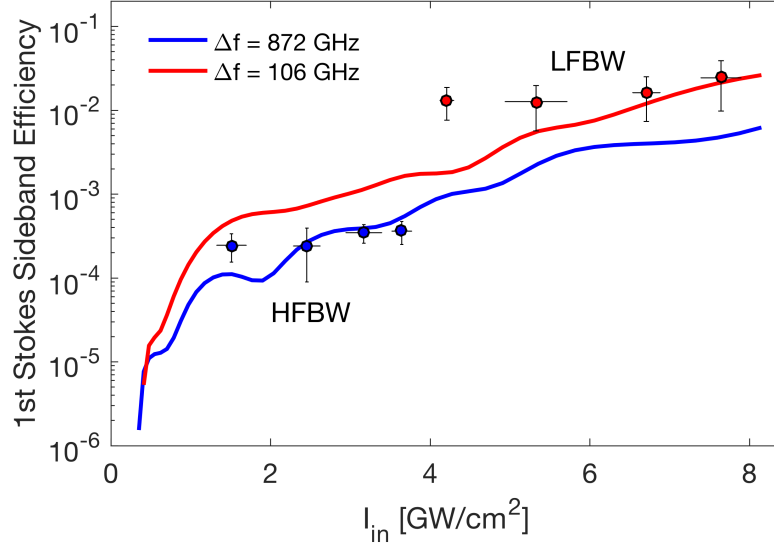
29

Figure 20: Simulation results modeling the efficiency of the 1st Stokes FWM sideband are shown in the blue and red lines for the HFBW and LFBW, respectively. Experimental data for each beat-wave is indicated by dots of the same color.

Rabi structure.

The calculations attribute the majority of the sideband light to a two step process where carriers are generated nonresonantly and subsequently accelerated through the BZ to high-k states by the strong electric field of the laser. Since the bands are nonparabolic, this changes the effective mass of the carriers and thus their contribution to the optical nonlinearity. As mentioned, current sources manifest as odd orders of the nonlinear optical susceptibility, leading not only to FWM sidebands but also odd harmonic generation (not studied in experiment). The same calculation is performed setting the intraband acceleration term to zero, shown as the dashed line in Fig. 21; the drastically reduced FWM efficiency for all intensities confirms the emission is generated primarily by currents. Note that at very low intensities (¡ 100 MW/cm^2), the two curves merge, showing that the free carrier effects begin to play a significant role in the nonlinear optical response of GaAs only at or above 1 GW/cm^2.

The beat-wave enhancement in this model can be explained by the bias time of the electric field - driving currents through the BZ is more efficient for lower frequency light, as
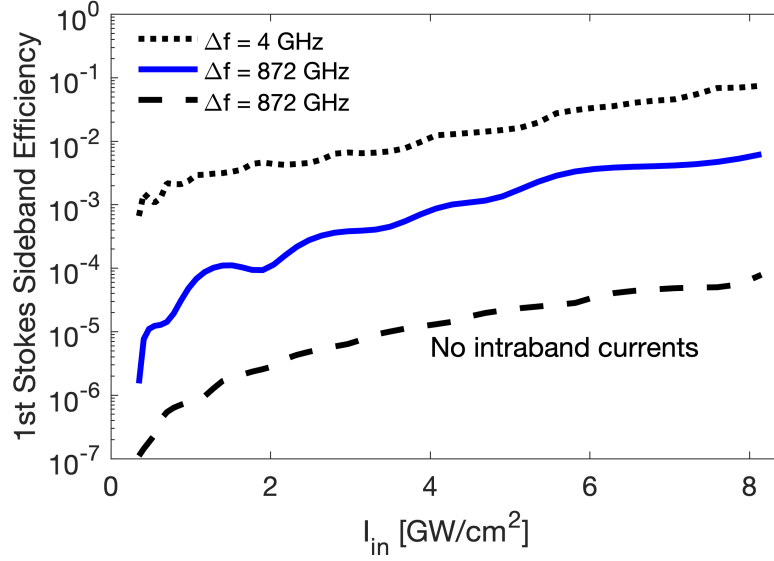
Figure 21: Extrapolation of the beat-wave enhancement of the Kerr nonlinearity in simulations. The dashed line indicates simulations with intraband currents disabled, disallowing any nonlinear current contribution to sideband generation.

the acceleration is "on" in one direction for a longer time. The same applies to the beat-wave - a lower frequency beat-wave will drive carriers to higher-k states and generate sideband light more efficiently. This concept is tested in simulations by further decreasing the laser beat frequency to 4 GHz, where the half-cycle bias time is 125 ps. This case is shown in Fig. 21, and shows even higher efficiency FWM than the cases tested in experiment, approaching two orders of magnitude higher nonlinear optical response than the HFBW. This enhancement corresponds to almost 10x increase in $n_{2,\text{eff}}$ simply by decreasing the beat-frequency of a CO_2 laser beat-wave. It is important to note that there is a temporal limitation on this enhancement, as the length of the pulse must be on the order of the beat period or longer for any enhancement to take place.

A similar type of beat-wave control of the nonlinear response of bulk semiconductors has been demonstrated using resonant interactions or heavily doped samples such as p-GaAs or n-GaAs irradiated by a CO_2 laser beat-wave [37, 38]. FWM efficiency was increased corresponding to a ~5x larger $n_{2,\text{eff}}$ than that previously measured [4]. This effect was

31

attributed to high-density electron distributions dissipating energy into the lattice modulated at the beat frequency. However these samples experienced extremely high loss (e.g. p-GaAs absorption was 5000 cm^{-1} at 10μm [38]) necessitating short propagation lengths ($\leq 200\mu$m) and thus impractically small conversion efficiencies. The theory developed in these papers does not consider any dynamic nonequilibrium processes and cannot accurately describe the physics we measure in GaAs.

6   Conclusion

In this thesis we have presented experimental measurements of the nonlinear refractive index in GaAs, n-Ge, and ZnSe using four-wave mixing of CO_2 laser beat-waves at both 1-10 GW/cm^2 and 1-10 MW/cm^2. Reasonable agreement is found between the values measured here and those measured in the literature using different wavelengths and experimental techniques. We also observe that the efficiency of the four-wave mixing process increases dramatically when decreasing the beat-frequency of the beat-waves, leading to a 10x increase in the nonlinear optical response. Calculations using the semiconductor Bloch equations attribute the growth of the nonlinearity to free carrier currents driven to nonparabolic regions of the Brillouin zone.

Calculations predict that lowering the beat frequency even further to 4 GHz can result in almost a 100x increase in the nonlinear optical response above that measured in the 872 GHz case, demonstrating the ability to control $n_{2,\text{eff}}$ of GaAs over a wide range by changing only the laser parameters. Very small beat-frequencies on the order of 10-100 MHz can be obtained at 10 μm by using acousto-optic modulators. Note that this would require 10s of ns long pulses at GW/cm^2 intensities, resulting in prohibitively high fluences greater than 10 J/cm^2. However it may be possible to approach beat-frequencies on the order of 1-10 GHz by oscillating simultaneously on the regular and sequence bands of the CO_2 laser [39], which should provide strong enhancement as shown.

The beat-wave control of the nonlinear susceptibility in GaAs may prove useful for a

variety of applications. In particular, the generation of a high power broadband spectrum in the long-wave infrared atmospheric transmission window may be possible, as sideband efficiency scales as $n_{2,\text{eff}}^2$. This would form a frequency comb and may be useful for remote sensing or high resolution spectroscopy applications in the LWIR.

Appendices

A. CaF$_2$ Attenuator Calibrations

CaF$_2$ windows were used throughout the experiments described in this thesis to attenuate 10μm laser beams in front of sensitive detectors, as well as increase their effective dynamic range when measuring beam profiles or sideband energies. Because of this, the calibration of the attenuation factor for windows of various thicknesses is of critical importance.

We measured incident and transmitted energy from each of our windows with the two intense wavelengths we had easy access to, $\lambda = 10.59$ and $\lambda = 10.27$. The attenuation factors A are given in Table 3 in the form $I_{in} = A I_{trans}$, so that a larger attenuation factor means stronger attenuation. An absorption coefficient α is found by plotting the measured transmission data against length and fitting it with Transmission $= \frac{I_{trans}}{I_{in}} = e^{-\alpha L}$ as shown in Fig. 22.

| | **Wavelength (μm)** | |
Thickness	10.27	10.59
2 mm	1.76	2.03
3 mm	2.50	3.13
6 mm	5.56	9.05
8 mm	9.58	21.1
12.7 mm	33.6	105

Table 3: Measured attenuation factors for CaF$_2$ windows used in four-wave mixing experiments.

Our measured value of α was found to be in good agreement with a value taken from a Corning Incorporated data sheet on the material [40]. The absorption coefficient was assumed to vary linearly with wavelength in our wavelength range of interest. Attenuation factors for each CaF$_2$ window are given in Table 4 for all of the FWM sideband wavelengths used in this thesis.
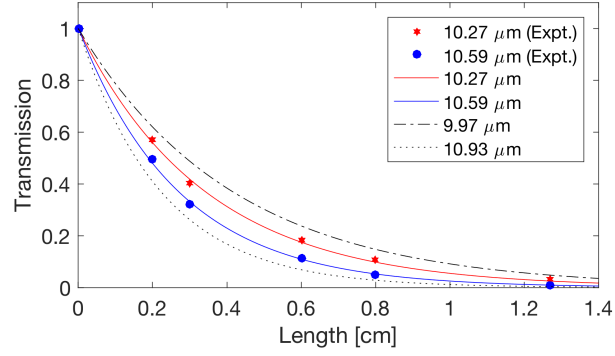
Figure 22: Transmission through different lengths of CaF$_2$ with different CO$_2$ laser wavelengths. The dotted/dashed lines are FWM sidebands with transmission calculated via a fitting described in Fig. 23.
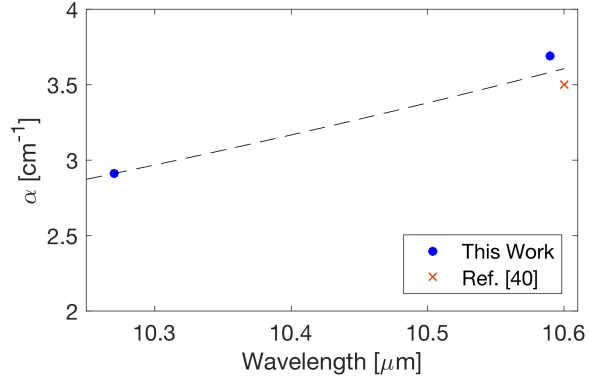

Figure 23: Fitting of the absorption coefficient of CaF$_2$. It was measured to be $\alpha = 3.7$ cm^{-1} at λ = 10.59 μm and $\alpha = 2.9$ cm^{-1} at $\lambda = 10.27$ μm.

	Wavelength (μm)							
Thickness	9.97	10.93	10.437	10.476	10.514	10.551	10.633	10.674
2 mm	1.611	2.043	1.91	1.94	1.97	2.01	2.08	2.12
3 mm	2.05	3.82	2.65	2.71	2.78	2.85	3.02	3.11
6 mm	4.21	14.6	7.00	7.36	7.73	8.13	9.12	9.68
8 mm	6.79	35.7	13.4	14.3	15.3	16.3	19.1	20.6
12.7 mm	20.9	290	61.4	68.3	75.9	84.3	108	122

Table 4: Extrapolated attenuation factors for CaF$_2$ windows used in four-wave mixing experiments.
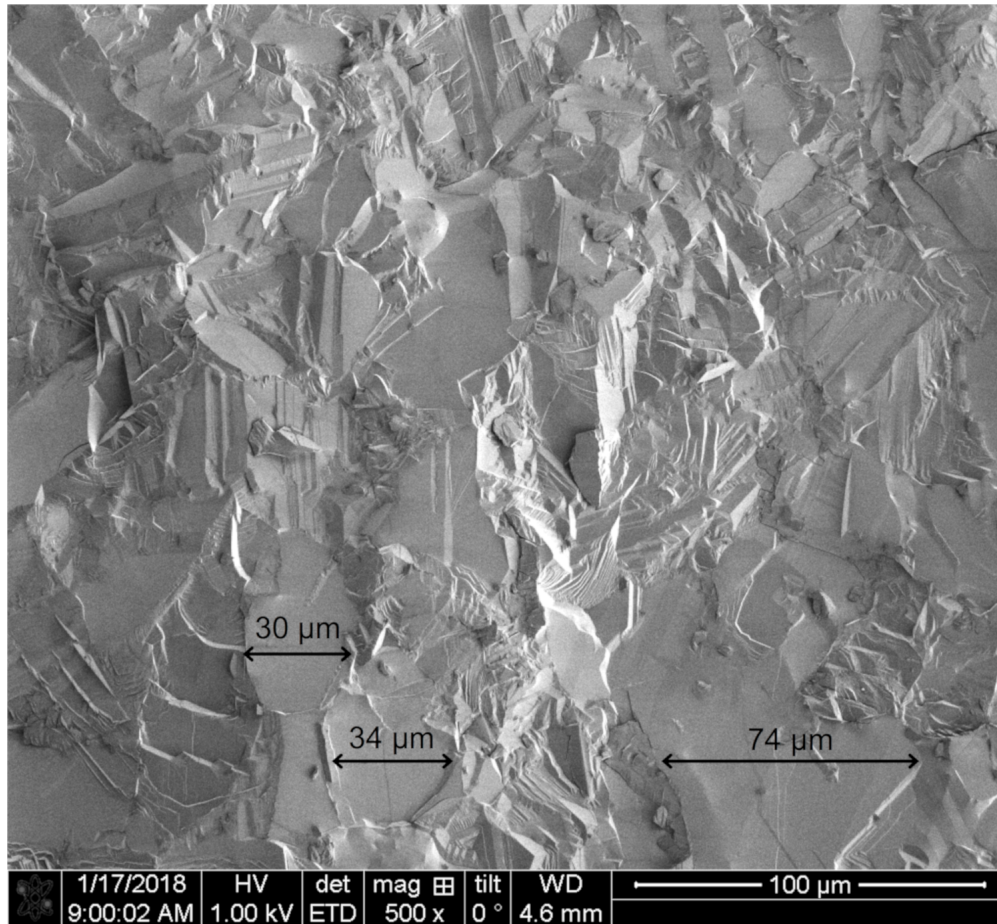
B. ZnSe Grain Size

Figure 24: Scanning electron microscope (SEM) image of a coarsely cleaved polycrystalline ZnSe sample. The grain size was estimated by measuring different flat regions on several different SEM images, examples of which are shown here, resulting in grains with an average dimension of 43 ± 15 μm. The cleaved sample was not used in four-wave mixing experiments, but is characteristic of the samples used in experiment, all grown for similar optical applications.

References

[1] S. Schmitt-Rink, D. Chemla, and D. Miller, "Linear and nonlinear optical properties of semiconductor quantum wells", Adv. Phys. **38**, 89 (1989).

[2] M. Sheik-Bahae, D. C. Hutchings, D. J. Hagan, and E. W. Van Stryland, "Dispersion of bound electronic nonlinear refraction in solids", IEEE J. Quantum Electron. **27**, 1296 (1991).

[3] J. J. Wynne, "Optical third-order mixing in GaAs, Ge, Si, and InAs", Phys. Rev. **178**, 1295 (1969).

[4] C. K. N. Patel, R. E. Slusher, and P. A. Fleury, "Optical nonlinearities due to mobile carriers in semiconductors", Phys. Rev. Lett. **17**, 1011 (1966).

[5] A. P. Jauho and K. Johnsen, "Dynamical Franz-Keldysh effect", Phys. Rev. Lett **76**, 4576 (1996).

[6] A. Srivastava, R. Srivastava, J. Wang, and J. Kono, "Laser-induced above-band-gap transparency in GaAs", Phys. Rev. Lett. **93**, 157401 (2004).

[7] S. M. Golin, S. E. Kirkwood, D. D. Klug, D. M. Villeneuve, D. M. Rayner, C. A. Trallero-Herrero, and P. B. Corkum, "Strong field processes inside gallium arsenide", J. Phys. B **47**, 204025 (2014).

[8] C. Schmidt, J. Buhler, A.-C. Heinrich, J. Allerbeck, R. Podzimski, D. Berghoff, T. Meier, W. G. Schmidt, C. Reichl, W. Wegscheider, D. Brida, and A. Leitenstorfer, "Signatures of transient Wannier-Stark localization in bulk gallium arsenide", Nat. Commun. **9**, 2890 (2018).

[9] O. Schubert, M. Hohenleutner, F. Langer, B. Urbank, C. Lange, U. Huttner, D. Golde, T. Meier, M. Kira, S. W. Koch, and R. Huber, "Sub-cycle control of terahertz high-harmonic generation by dynamical Bloch oscillations", Nat. Photon. **8**, 119 (2014).

[10] S. Ghimire, A. D. DiChiara, E. Sistrunk, P. Agostini, L. F. DiMauro, and D. A. Reis, "Observation of high-order harmonic generation in a bulk crystal", Nat. Phys. **7**, 138 (2011).

[11] M. Hohenleutner, F. Langer, O. Schubert, M. Knorr, U. Huttner, S. W. Koch, M. Kira, and R. Huber, "Real-time observation of interfering crystal electrons in high-harmonic generation", Nature **523**, 572 (2015).

[12] G. Vampa, T. J. Hammond, N. Thire, B. E. Schmidt, F. Legare, C. R. McDonald, T. Brabec, and P. B. Corkum, "Linking high harmonics from gases and solids", Nature **522**, 462 (2015).

[13] O. D. Mucke, T. Tritschler, M. Wegener, U. Morgner, and F. X. Kartner, "Signatures of carrier-wave Rabi flopping in GaAs", Phys. Rev. Lett. **87**, 057401 (2001).

[14] F. Junginger, B. Mayer, C. Schmidt, O. Schubert, S. Mahrlein, A. Leitenstorfer, R. Huber, and A. Pashkin, "Nonperturbative interband response of a bulk InSb semiconductor driven off resonantly by terahertz electromagnetic few-cycle pulses", Phys. Rev. Lett. **109**, 147403 (2012).

[15] R. W. Boyd, *Nonlinear Optics*, 3rd (Academic Press, 2008).

[16] N. Bloembergen, *Nonlinear Optics*, 4th (World Scientific, 1996).

[17] L. V. Keldysh, "Ionization in the field of a strong electromagnetic wave", Sov. Phys. JETP **20**, 1307 (1965).

[18] C. Kittel, *Introduction to Solid State Physics*, 7th (John Wiley & Sons, Inc., 1996).

[19] A. Miller, D. A. B. Miller, and S. D. Smith, "Dynamic non-linear optical processes in semiconductors", Adv. Phys. **30**, 697 (1981).

[20] P. A. Wolff and G. A. Pearson, "Theory of optical mixing by mobile carriers in semiconductors", Phys. Rev. Lett. **17**, 1015 (1966).

[21] V. G. Dmitriev, G. G. Gurzadyan, and D. N. Nikogosyan, *Handbook of Nonlinear Optical Crystals* (Springer, 1999).

[22]C. V. Filip, R. Narang, S. Y. Tochitsky, C. E. Clayton, and C. Joshi, "Optical Kerr switching technique for the production of a picosecond, multiwavelength CO_2 laser pulse", Appl. Opt. **41**, 3743 (2002).

[23]E. D. Capron and O. L. Brill, "Absorption coefficient as a function of resistance for optical germanium at 10.6 μm", Appl. Opt. **12**, 569 (1973).

[24]S. Y. Yuen, R. L. Aggarwal, N. Lee, and B. Lax, "Nonlinear absorption of CO_2 laser radiation by nonequilibrium carriers in germanium", Opt. Commun. **28**, 237 (1979).

[25]S. E. Trubnick, "Development of teflon bonding technology for nonlinear optical gallium arsenide devices", M.S. thesis (University of California Los Angeles, 2007).

[26]C. C. Wang and N. W. Ressler, "Observation of optical mixing due to conduction electrons in n-type germanium", Phys. Rev. B **2**, 1827 (1970).

[27]M. N. Polyanskiy, M. Babzien, and I. V. Pogorelsky, "Chirped-pulse amplification in a CO_2 laser", Optica **2**, 675 (2015).

[28]K. Werner, M. G. Hastings, A. Schweinsberg, B. L. Wilmer, D. Austin, C. M. Wolfe, M. Kolesik, T. R. Ensley, L. Vanderhoef, A. Valenzuela, and E. Chowdhury, "Ultrafast mid-infrared high harmonic and supercontinuum generation with n_2 characterization in zinc selenide", Opt. Express **27**, 2867 (2019).

[29]W. C. Hurlbut, Y.-S. Lee, K. L. Vodopyanov, P. S. Kuo, and M. M. Fejer, "Multiphoton absorption and nonlinear refraction of GaAs in the mid-infrared", Opt. Lett. **32**, 668 (2007).

[30]A. A. Said, M. Sheik-Bahae, D. J. Hagan, T. H. Wei, J. Wang, J. Young, and E. W. Van Stryland, "Determination of bound-electronic and free-carrier nonlinearities in ZnSe", J. Opt. Soc. Am. B **9**, 405 (1992).

[31]D. C. Hutchings and B. S. Wherrett, "Theory of the anisotropy of ultrafast nonlinear refraction in zinc-blende semiconductors", Phys. Rev. B **52**, 8150 (1995).

[32]T. J. Bridges and A. R. Strnad, "Submillimeter wave generation by difference-frequency mixing in GaAs", Appl. Phys. Lett. **20**, 382 (1972).

[33]D. Matteo, J. Pigeon, S. Tochitsky, U. Huttner, M. Kira, S. W. Koch, J. V. Moloney, and C. Joshi, "Control of the nonlinear response of bulk GaAs induced by long-wavelength infrared pulses", submitted to Optica, 2019.

[34]T. Kinsel and I. Kudman, "Carrier recombination in Gallium Arsenide", Solid State Electron. **8**, 797 (1965).

[35]M. Kira and S. W. Koch, *Semiconductor Quantum Optics* (Cambridge University Press, 2012).

[36]H. Haug and S. W. Koch, *Quantum Theory of the Optical and Electronic Properties of Semiconductors* (World Scientific, 2009).

[37]S. Y. Yuen, P. A. Wolff, L. R. Ram-Mohan, and R. A. Logan, "Hole induced four wave mixing and intervalence band relaxation times in p-GaAs and p-Ge", Solid State Commun. **56**, 489 (1985).

[38]S. Y. Auyang and P. A. Wolff, "Free-carrier-induced third-order optical nonlinearities in semiconductors", J. Opt. Soc. Am. B **6**, 595 (1989).

[39]V. O. Petukhov, S. Ya. Tochitsky, and V. V. Churakov, "Efficient simultaneous stimulated emission of two lines in different sequence bands in a TEA CO_2 laser", Sov. J. Quantum Electron. **17**, 389 (1987).

[40]*Calcium Fluoride CaF_2 Physical and Chemical Properties*, Published by Corning Incorporated: https://lightmachinery.com/media/1542/h0607_caf2_product_sheet.pdf, Oct. 2003.